Complementary slip distributions of the largest earthquakes in the 2012 Brawley swarm, Imperial Valley, California

Shengji Wei,[1] Don Helmberger,[1] Susan Owen,[2] Robert W. Graves,[3] Kenneth W. Hudnut,[3] and Eric J. Fielding[2]

Received 20 December 2012; revised 12 February 2013; accepted 14 February 2013; published 14 March 2013.

[1] We investigate the finite rupture processes of two $M > 5$ earthquakes in the 2012 Brawley swarm by joint inversion of nearby strong motion and high-rate GPS data. Waveform inversions up to 3 Hz were made possible by using a small event (M_w3.9) for path calibration of the velocity structure. Our results indicate that the first (M_w5.3) event ruptured a strong, concentrated asperity with offsets of ~20 cm centered at a depth of 5 km. The subsequent M_w5.4 event occurred 1.5 h later with a shallower slip distribution that surrounds and is complementary to that of the earlier event. The second event has a longer rise time and weaker high-frequency energy release compared to the M_w5.3 event. Both events display strong rupture directivity toward the southwest and lack of very shallow (<2 km) coseismic slip. The hypocenters for these events appear to be near or in the bedrock, but most of the slip is distributed at shallower depths (<6 km) and can explain a large part of the GPS offsets for the swarm. The complementary slip distributions of the two events suggest a triggering relationship between them with no significant creep needed to explain the various data sets. **Citation:** Wei, S., D. Helmberger, S. Owen, R. W. Graves, K. W. Hudnut, and E. J. Fielding (2013), Complementary slip distributions of the largest earthquakes in the 2012 Brawley swarm, Imperial Valley, California, *Geophys. Res. Lett.*, *40*, 847–852, doi:10.1002/grl.50259.

1. Introduction

[2] Earthquake swarms are sequences of events that lack a clear mainshock and fail to decay in time according to standard aftershock scaling laws. They have been commonly observed along active transform plate boundaries and in regions associated with volcanic activity, such as the Kilauea volcano in Hawaii, Reykjanes Peninsula in Iceland, and Miyake-jima in Japan [*Hill*, 1977; *Klein et al*., 1977; *Toda et al*., 2002]. Magma intrusion and fluid fluctuations have been proposed as possible driving factors to generate earthquake swarms [*Hill*, 1977; *Vidale et al*., 2006]. Recent deployment of dense seismic networks has led to the development of high-quality earthquake catalogues and, consequently, more earthquake swarms have been documented, especially in Japan and Southern California [*Ide*, 2001; *Vidale and Shearer*, 2006; *Vidale et al*., 2006]. The spatial and temporal patterns of the swarms have also been studied and reveal migration velocities ranging from 0.008 to 1.0 km/h [*Chen and Shearer*, 2011; *Roland and McGuire*, 2009]. This leads to a characteristic of earthquake swarms in more general terms as occurring over a relatively large spatial area relative to their total seismic moment, with stress drops of swarm events typically yielding lower values compared with other common earthquakes [*Chen and Shearer*, 2011; *Hardebeck and Aron*, 2009]. Many of these previous studies treat individual swarm events as point sources occurring at their hypocenters, which can make it difficult to understand triggering mechanisms among the swarm events and their relationship with creep during the swarm process.

[3] In recent years, geodetic techniques have been used in combination with seismological data to better understand the faulting behavior of earthquake swarms in Japan, California, Sierra Nevada, Yellowstone, and the East African Rift [*Baer et al*., 2008; *Bell et al*., 2012; *Wicks et al*., 2011]. The static moment obtained by geodetic data is usually larger than the total coseismic moment and thus aseismic creep has been proposed as one mechanism to account for this discrepancy [*Lohman and McGuire*, 2007; *Wicks et al*., 2011]. However, because earthquake swarms have many events occurring over a short period of time [*Benoit and McNutt*, 1996], it can be difficult to isolate the static signal produced by individual events in the swarm using geodetic tools such as interferometric synthetic aperture radar (InSAR) or traditional GPS with daily solutions. However, high-rate GPS in combination with seismic data offers the potential to image the rupture details and deformation associated with individual events along with the larger-scale deformation of the entire swarm process.

[4] The Brawley region is well known for its high geothermal activity [*Lynch and Hudnut*, 2008], and earthquake swarms have been observed in this region for many years [*Hauksson et al*., 2013]. The most recent swarm activity, referred to as the 2012 Brawley swarm hereafter, occurred about 20 km to the south of the 2005 swarm along the Brawley seismic zone (Figure 1). The swarm started on 26 August 17:02:12.7 UTC (first $M > 3.5$ event) and lasted for about 36 h (the last $M > 3.5$ event). All the events with M_w greater than 3.5 are displayed in time series in Figure 1b. Two of these events have a magnitude larger than 5.0; Southern California Seismic Network event IDs of 15199681 (M_w5.3) and 15200401 (M_w5.4); and account for over 70% of the total seismic moment released during the swarm. The M_w5.3 event occurred about 1.5 h before the M_w5.4 event.

All Supporting Information may be found in the online version of this article.

[1]Geological and Planetary Sciences, California Institute of Technology, Pasadena, California, 91125, USA.
[2]Jet Propulsion Laboratory, California Institute of Technology, Pasadena, California, USA.
[3]U.S. Geological Survey, Pasadena, California, USA.

Corresponding author: S. Wei, Geological and Planetary Sciences, California Institute of Technology, Pasadena, CA 91125, USA. (shjwei@gmail.com)

0094-8276/13/10.1002/grl.50259

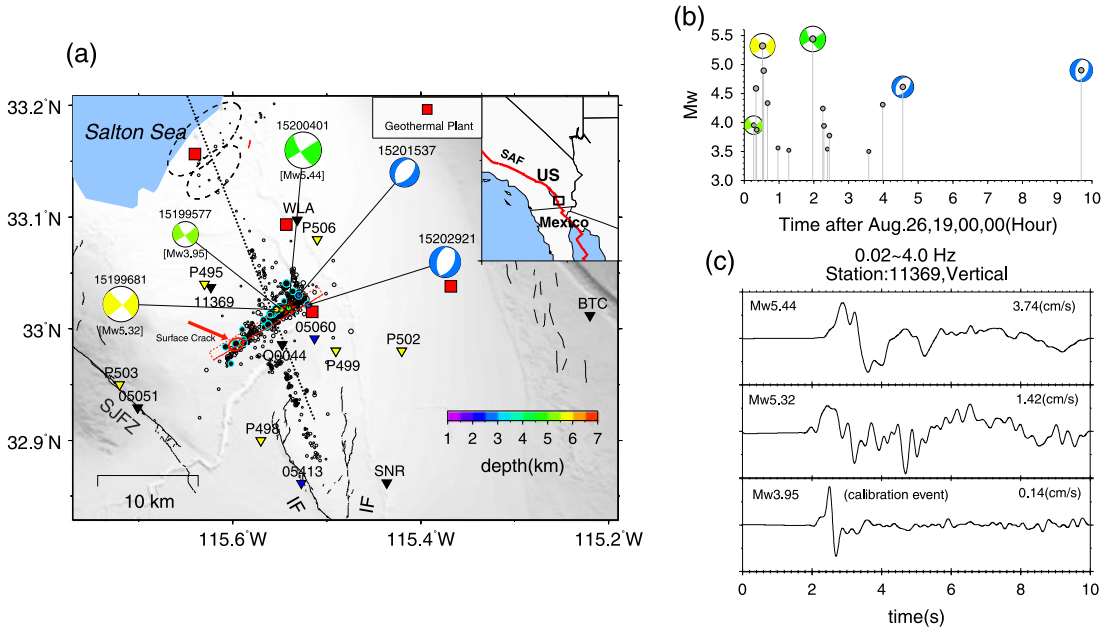

Figure 1. Overview of the swarm. (a) The larger map shows relocated seismicity of the 2012 Brawley swarm (black dots) [*Hauksson et al.*, 2013]. The epicenter of the largest event (M_w5.4) is shown as a red star and the fault plane is displayed as a rectangle. The mechanisms of five events are displayed. The triangles are the strong motion (black and blue) and GPS (yellow) stations. The two blue stations only recorded the M_w5.3 event. The two ellipses indicate the 2005 (larger) and 1987 (smaller) swarms. The heavy dashed line indicates the Brawley Seismic Zone. IF, SJFZ, and SAF indicate the Imperial Fault, San Jacinto Fault Zone, and San Andreas Fault, respectively. (b) 10 h time series of the swarm for the events with $M > 3.5$, the same five mechanisms as in Figure 1a are shown. (c) 0.02 ~ 4.0 Hz velocity waveforms at strong motion station 11369 for event 15199577, 15199681, and 15200401. The peak amplitude is indicated at the end of each record. Note the source complexity of the two $M > 5$ events.

[5] Many of the swarm events were well recorded by strong motion stations in the Imperial Valley (Figure 1a). To better recognize the complexity of the source process of the largest events, Figure 1c compares the vertical velocity waveforms recorded at one of the closest strong motion stations (11369) for the $M > 5$ events and a M_w3.9 event (ID 15199577). Due to the extremely slow near-surface velocities, the seismic wave incidence at this site is nearly vertical, isolating the *P* waves on the vertical component (*S* wave arrival time is about 5 s). The waveform of the smaller event is simple, whereas the waveforms for the $M > 5$ events are much more complex. Because the hypocenters of three events are located within 2 km of one another, we attribute the waveform complexity to source processes instead of path effects. This suggests the smaller M_w3.9 earthquake can be used to calibrate local site velocity models, which can be used for finite fault inversion of the larger events.

1.1. Path Calibration

[6] The Imperial Valley is known for its thick accumulation of sedimentary and meta-sedimentary rocks, reaching depths of about 5.5 km in the middle of the basin where the swarm occurred [*Fuis et al.*, 1984]. To model the ground motions of the M_w3.9 calibration event, we extracted 1-D velocity profiles from the Southern California Earthquake Center 3-D velocity models for Southern California; i.e., CVM4.0 and CVM_H11.9.0 [*Magistrale et al.*, 2000; *Plesch et al.*, 2009] as shown in Figure 2a for station 11369. The upper panels of Figure 2c compare observed three-component waveforms at station 11369 with those simulated using these extracted 1-D models. Here we align the synthetics and data on the *P* wave first arrival to account for possible origin time error (similar procedure is utilized in the following finite fault inversion). As shown, these initial models cannot match the timing or waveform of the *S* wave motions on the horizontal components, which we interpret to be caused by inaccuracies in the shallow velocity structure.

[7] To calibrate the shallow velocity structure in our 1-D profiles, we used two parameters, *Vp*_min (velocity at the surface) and D_vp4.0 (the depth where *Vp* reaches 4.0 km/s). The relation $Vs = (Vp - 1.36)/1.16$ is used to link *Vs* with *Vp* when $Vp < 4.0$ km/s (Figure 2b). This equation was derived from a linear regression of borehole and VSP measurements for clay-rich sedimentary rocks [*Brocher*, 2005]. A constant *Vs*/*Vp* ratio of 1.73 is used for $Vp > 4.0$ km/s. We then conducted a grid search for the best parameter combinations that can fit both the *P* and *S* wave arrival times. One example velocity profile is displayed in Figure 2a, with corresponding waveform fits shown in Figure 2c. The obvious improvements in both travel time and waveforms show the sensitivity of our parameter setup. See Figure S1 for the calibration models for other strong motion stations. Our results indicate that stations 11369, 05060, 05013, and SNR, which are located in the middle of the basin, favor the same 1-D velocity model, referred to as the path calibration model (PCM) shown in Figure 2a. Stations closer to the edge of the basin have faster average velocities, and the sediment ($Vp < 4.0$ km/s) is thinner than PCM, consistent with active source imaging results [*Fuis et al.*, 1984]. Velocity models for stations Q0044 and WLA are slightly different than PCM; mainly due to the local microbasin structure for

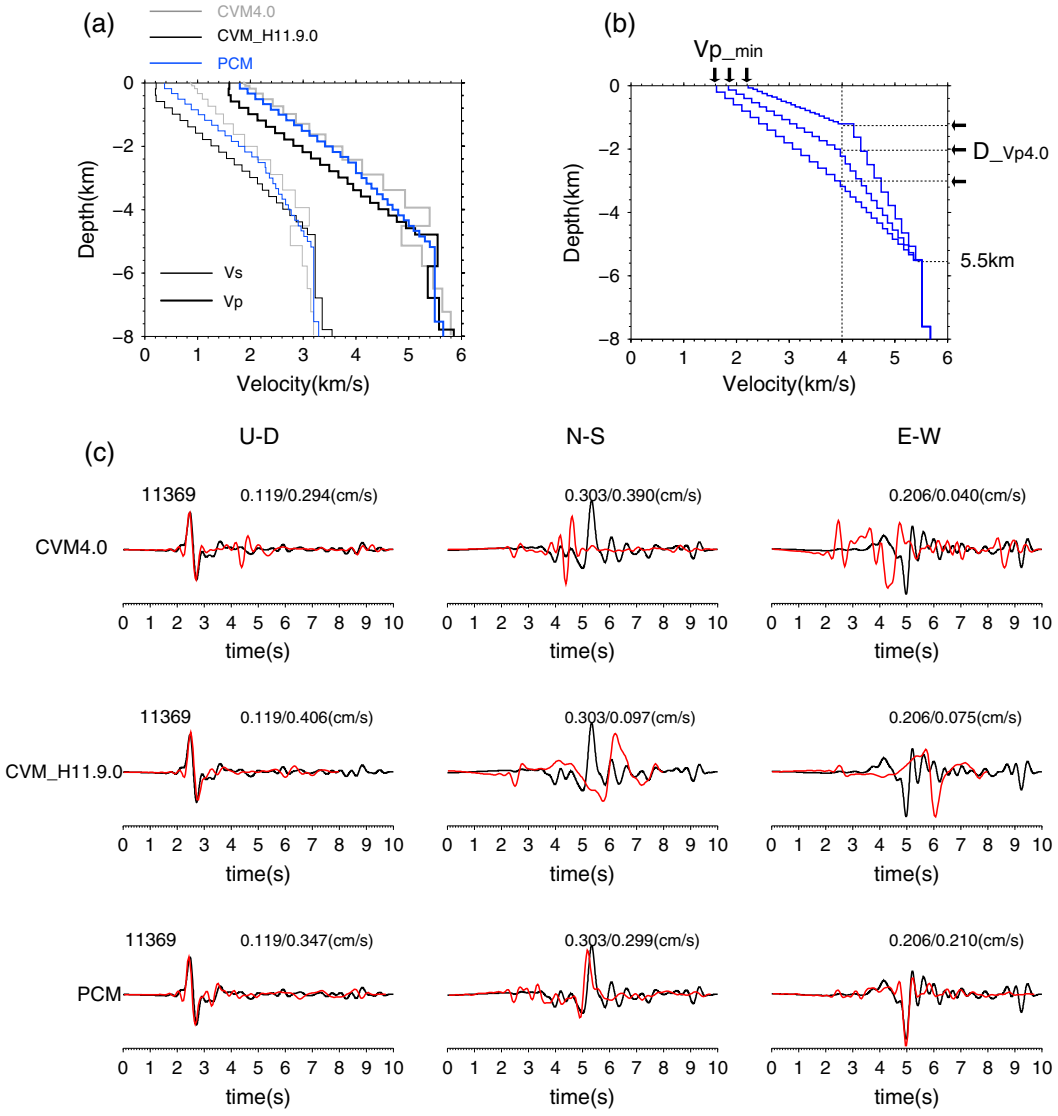

Figure 2. 1-D velocity models and synthetics for the M_w3.9 calibration event. (a) *Vs* and *Vp* depth profiles for the path calibration model (PCM) and the two 1-D profiles extracted from the CVM4.0 and CVM_H11.9.0 3-D velocity models at the location of epicenter of the M_w5.4 event. (b) Schematic velocity profiles indicating how to obtain a calibrated velocity model. Depth of the sediment base is fixed at 5.5 km, the *Vp*_min and *D*_vp4.0 are the two variable parameters during a grid search. (c) Three-component waveform comparison between the data (black) and the synthetics (red). Here the synthetics are computed using the three velocity models in Figure 2a. Both data and synthetics are filtered to 0.02 ~ 3.0 Hz. The peak amplitudes of data (first) and synthetic (second) are shown.

example WLA is sitting on an old river delta and favors a very slow *Vs* layer at the surface (Figure S1).

1.2. Inversion Setup

[8] We assume a rectangular fault as indicated in Figure 1a. We initially use the strike (239°) and dip (90°) from the best point source mechanism derived from joint inversion of local and teleseismic waveforms [*Chen et al.*, 2012; *Chu and Helmberger*, 2013], and allowed some perturbations to better fit the data. While the strike remains the same, we found that a dip of 85° does a slightly better job and we use these values for both the M_w5.4 and M_w5.3 events. For our modeling, we assume these two events occurred along the same fault, based on the similarity of their mechanisms and their approximate epicentral locations (Figure 1). The relocated hypocenters were used in the inversion [*Hauksson et al.*, 2013]. We divide the fault plane into subfaults, with dimensions of 0.75 km*0.75 km. On each subfault, we simultaneously invert for slip, rake, rise time, and average rupture velocity using a simulated annealing algorithm [*Ji et al.*, 2002]. During the inversion, we allow the slip amplitude to vary from 0 to 80 cm, while the rupture velocity can range between 2.0 and 3.0 km/s.

[9] The data used in inverting the M_w5.4 earthquake include 6 strong motion stations (SNR, 05051, WLA, BTC, Q0044, 11369) and 4 high-rate GPS stations (P498, P499, P502 P506). Both the data and Green's functions are bandpass filtered between 0.1 and 3 Hz. Due to the relatively weak long period energy radiation of the M_w5.3 event, the high-rate GPS data are not of sufficient quality to be used in the inversion for this event. Fortunately, there are two additional strong motion stations (05060, 05413) that recorded the M_w5.3 event (Figure 1a). Generally, static offset

data prove particularly useful in defining the slip distribution for large complex ruptures such as the M_w7.2 El Mayor-Cucapah event [*Wei et al.*, 2011]. Unfortunately, use of the static GPS data alone for the present analysis is problematic due to the accumulated deformation of the swarm activity, and the relatively small magnitudes of the swarm events. However, combining the geodetic and seismic data in the analysis provides a powerful tool for examining the relative contributions of aseismic and coseismic deformation during the swarm process.

1.3. Inversion Results

[10] Our results are summarized in Figure 3 for both the earlier M_w5.3 event and the M_w5.4 event. Here we have included the 5 Hz GPS displacement waveforms and a sample of the strongest horizontal strong motion velocity waveforms for the M_w5.4 event. See Figures S2 and S3 for three-component waveform fits for all the stations. Both data sets are well-fit and no travel-time corrections are needed. The kinematic slip models for the M_w5.3 and M_w5.4 events are displayed in Figures 3b and 3c, respectively, with slip distributions shown in upper panels and smoothed rise times and rupture times shown in the lower panels. The moment distributions in time and depth are displayed in Figures 3d and 3e. Both events have very strong rupture directivity toward the southwest, and the M_w5.4 event lasted slightly longer than the M_w5.3 event (Figure 3d). The M_w5.4 event also displays a shallower and broader rupture area than the M_w5.3 event with maximum slip amplitudes of 40 and 30 cm, respectively. The differences in moment distribution with depth can be seen in Figure 3e. Note that the average depth of slip is above 4 km for the M_w5.4 in agreement with *Chu and Helmberger* [2013].

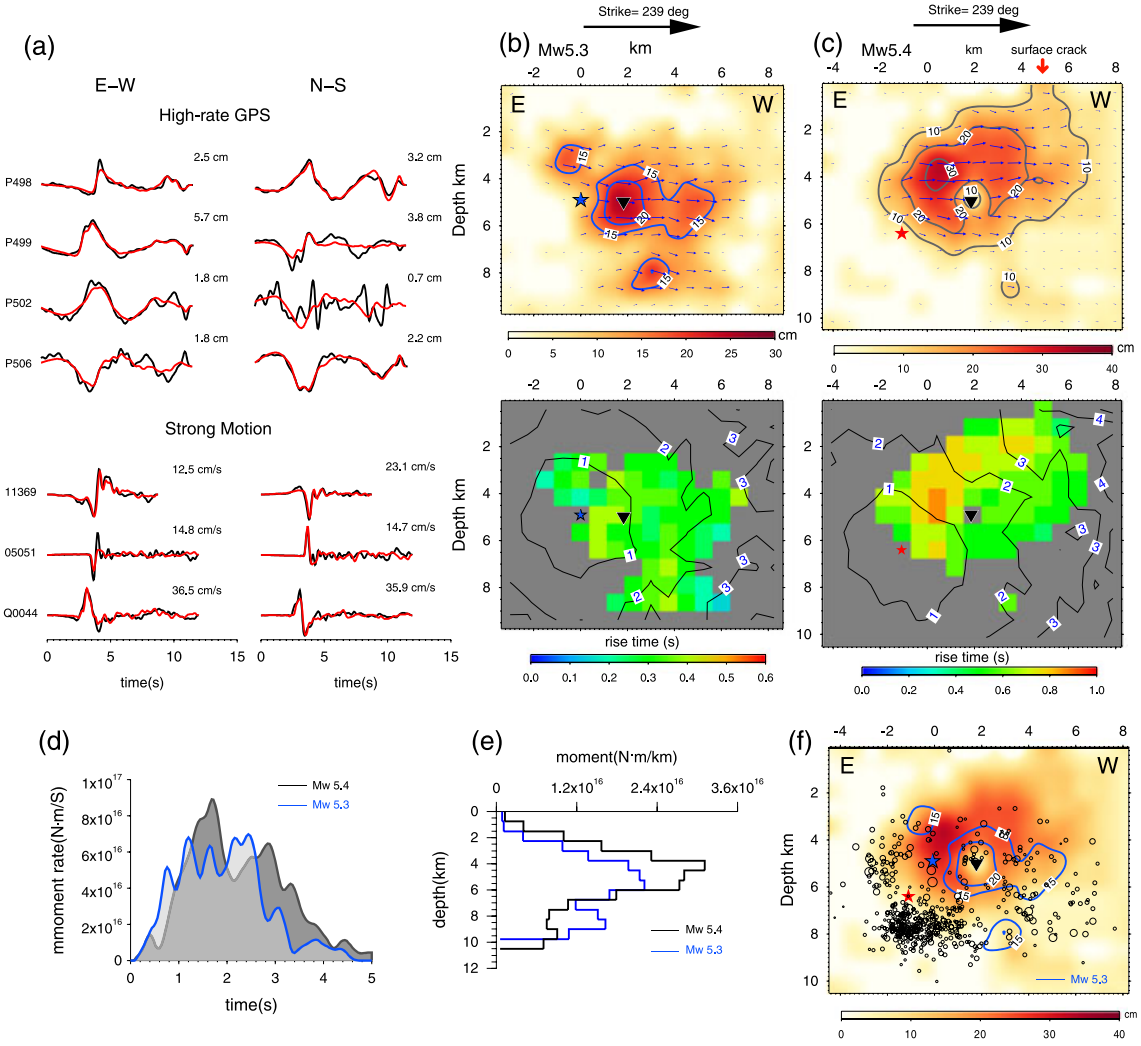

Figure 3. Slip models of the two $M > 5$ events. (a) The horizontal waveform comparisons of the high-rate GPS displacement waveforms (upper) and strong motion velocity waveforms (lower) for the M_w5.4 event. The synthetics (red) are generated using the preferred slip model for the M_w5.4 event. Both data and synthetics are filtered to 0.1 ~ 3.0 Hz. (b) Kinematic slip model for the M_w5.3 earthquake with the blue star shows the hypocenter location. Slip distribution is displayed in the upper panel, smoothed rise times and rupture times (contours) are shown in the lower panel. The black triangle is an indicator of the same place on the fault for better comparison. (c) Similar to Figure 3b for the M_w5.4 event. (d) Moment rate functions for both $M > 5$ events. (e) Moment distributions in depth. (f) Overlapping slip models, with color indicating slip distribution for the M_w5.4 event and the contours corresponding to the M_w5.3 earthquake. Relocated hypocenters of events near the fault (within 2 km) are projected on the fault (circles).

[11] When the slip distributions of the two events are overlain (Figure 3f), we observe strongly complementary slip distributions. Because the M_w5.3 event happened about 1.5 h ahead of the M_w5.4 event, we suspect the M_w5.4 event was triggered by the M_w5.3 event. The correspondence of the strong asperity for the M_w5.3 and the apparent hole in slip for the latter M_w5.4 is striking and one might wonder if such detail is resolvable. After conducting some complete checkerboard tests (Figure S4) we conclude this is a robust feature of these models, at least in a relative sense. Another complementary aspect of these events is that while the shallower M_w5.4 event favors longer rise times (~0.8 s on average, Figure 3b), the M_w5.3 event prefers smaller values (~0.4 s, Figure 3c). This is consistent with the results of *Kagawa et al.* [2004] who found larger effective stress drops and slip velocities for asperities deeper than 5 km compared with those for shallower ruptures. The larger event produces simpler waveforms because the largest slip patch (~30 cm) has a longer rise time and the radiation is quite uniform. In contrast, the M_w5.3 event has more complexity at shorter periods (Figures 1c, S2, and S3), which is also evident in the moment rate plots (Figure 3d). Figure 3f also compares the locations of the smaller swarm events with the slip distributions. We find that the smaller events occurred primarily around the edges and beneath the large slip patches, reinforcing the causal relationship among the swarm events.

2. Discussion

[12] One of the intriguing properties of swarms is the possibility of predicting the temporal and spatial evolution of the activity. For example, the theoretical study of repeating event behavior suggests a slip weakening zone can be influenced by failure on a nearby slip weakening zone [*Chen and Lapusta*, 2009]. The complementary slip distribution between two $M > 5$ events with just 90 min difference in origin time strongly suggests a triggering relationship between them. The driving mechanism could either be static stress loading [*King et al.*, 1994] and/or accelerating creep loading governed by rate-and-state friction laws [*Rubin*, 2008; *Segall et al.*, 2006]. The weak initiations of the two $M > 5$ events (Figure S5) at relatively deeper depth (>5 km) also suggest the imprint of a heterogeneous stress distribution on the fault, which could be related to the arrest of previous small events, and/or to stress concentrations at the sediment/bedrock interface [*Lapusta and Rice*, 2003].

[13] A competing argument for both stress loading and event migration rate hypotheses is aseismic slip [*Lohman and McGuire*, 2007], in which shallow creep drives the earthquake swarm. Here, the combination of space-geodesy and seismology can address this issue directly. The horizontal components of 48 h of GPS data (20 min samples) at the closest station (P499) are presented in Figure 4a, along with the temporal evolution of seismicity during the swarm. There is no clear creep signal 24 h before or after the $M > 5$ events, and the static offsets are predominantly related to the largest events, as indicated by their consistency with cumulative seismic moment. Examining these features in greater detail, the high-rate (5 Hz) channel data on the E-W component provides a clear view of the motions that occurred during the M_w5.4 event (Figure 4b). As shown, the dynamic and static signals produced by the M_w5.4 event are clearly above the noise level in the GPS data and the preferred kinematic

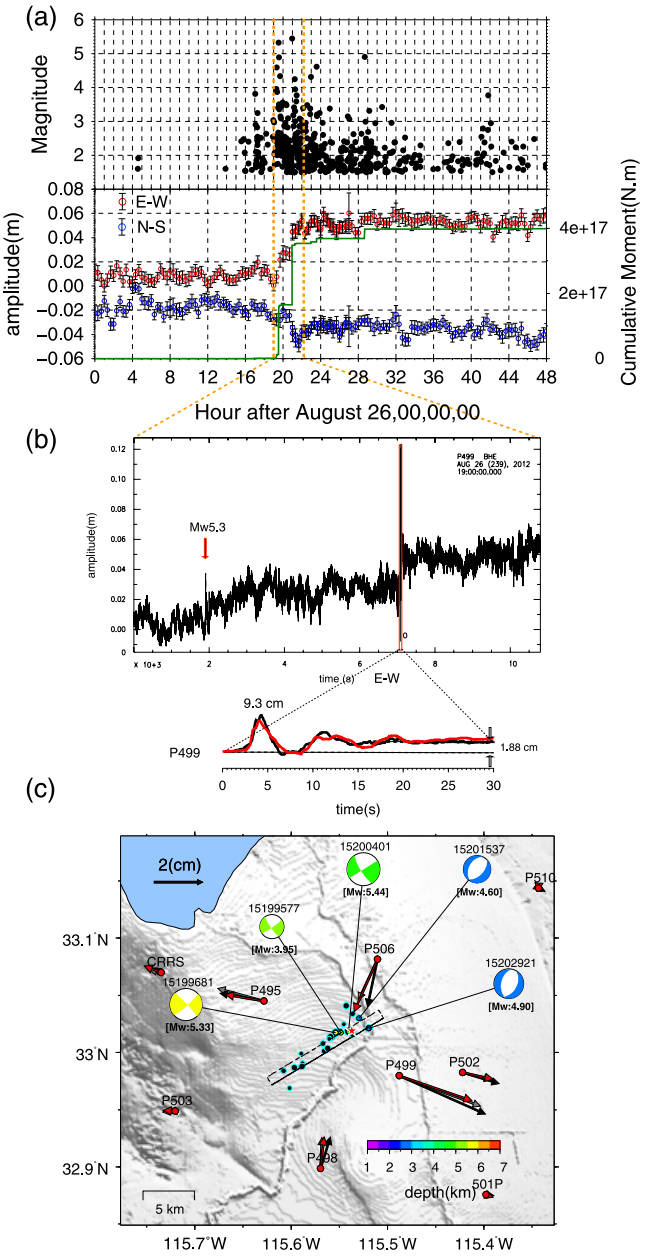

Figure 4. GPS data fitting. (a) 20 min resolution horizontal GPS data at station P499 (lower) and swarm seismicity (upper) in 48 h along with the cumulative seismic moment (heavy green). (b) E-W component of 5 Hz GPS record at station P499. 30 s record for the M_w5.4 event is enlarged and plotted with the synthetic generated from the preferred model. (c) The horizontal static offsets (black, USGS; gray, MIT) on nearby GPS stations are plotted along with the synthetics (red) produced by the total slip models of M_w5.3 and M_w5.4 events. Note that the data have been scale by a factor of 70% to account for the moment difference.

slip model can explain both quite well. Together the total synthetic static offsets generated by the slip models of the M_w5.3 and M_w5.4 events are compared with the observations in Figure 4c. Note that we scaled the GPS data down by 30% to adjust for the accumulated deformation from the other smaller events in the swarm (Figure 4a). The good agreement between the data and synthetics indicates that in this

case, the offsets are mostly coseismic and are not obviously correlated with deep creep processes. The small remaining misfit may be due to our exclusion of smaller events, including the M4.6 and M4.9 normal events (Figure 4c).

[14] The sensitivity of various data to very shallow slip (<2 km) is explored in Figure S6 where we calculated both static and seismic synthetics using a hypothetical shallow slip distribution. The simulated synthetics show much stronger surface waves than the data that are dominated by S waves, indicating it is unlikely that significant coseismic slip occurred along the very shallow (<2 km) portion of the fault. However, the simulated static deformation from this model at the GPS stations is quite small (because the deformation is concentrated very close to the fault) indicating that the existing GPS station configuration cannot rule out the possible occurrence of shallow aseismic creep. The broader spatial coverage of InSAR data, on the other hand, has better resolution for investigating the potential for shallow deformation. A pair of ascending and descending TerraSAR-X interferograms covering the time period of the swarm, processed with ROI_pac, are presented in Figure S7 with the predictions from our inverted slip models. The major patterns and peak amplitude in the data are well-fit by the synthetics, implying no significant shallow creep occurred. Some detailed features in the InSAR data, however, are not as well-fit. This may be due to complexity of the fault geometry and the excluded events as mentioned above for the GPS analysis. Although further work is needed to more fully explain the InSAR data, our current analysis indicates no significant shallow or deep creep occurred during the 2012 Brawley swarm.

3. Conclusion

[15] Joint inversion of strong motion and high-rate GPS data revealed complementary slip distributions between the two largest ($M > 5$) events in the 2012 Brawley swarm, suggesting a triggering relationship between them. Both events display strong rupture directivity toward the southwest. The M_w5.4 event has longer rise time than the M_w5.3 event and thus has weaker high-frequency energy. The two events both lack very shallow (<2 km) coseismic slip and no significant creep is needed to explain various data sets.

[16] **Acknowledgments**. The strong motion data were downloaded from the Southern California Seismic Network and USGS. The original TerraSAR-X data is copyright 2012 by the German space agency DLR, provided under the Group on Earth Observation Geohazard Supersite project. Part of this research was supported by the USGS grant G12AP20072, Caltech Tectonics Observatory, NASA Earth Surface and Interior focus area and performed at the JPL, Caltech. The high-rate GPS data were provided by the NSF PBO and archived at UNAVCO. Static offset GPS processing was performed by Jerry Svarc (USGS) and Tom Herring (MIT). The manuscript was improved by the constructive input of Karen Felzer, Gavin Hayes and two anonymous reviewers.

References

Baer, G., Y. Hamiel, G. Shamir, and R. Nof (2008), Evolution of a magma-driven earthquake swarm and triggering of the nearby Oldoinyo Lengai eruption, as resolved by InSAR, ground observations and elastic modeling, East African Rift, 2007, *Earth Planet. Sci. Lett.*, *272*(1–2), 339–352.

Bell, J. W., F. Amelung, and C. D. Henry (2012), InSAR analysis of the 2008 Reno-Mogul earthquake swarm: Evidence for westward migration of Walker Lane style dextral faulting, *Geophys. Res. Lett.*, *39*, doi:10.1029/2012GL052795.

Benoit, J. P., and S. R. McNutt (1996), Global volcanic earthquake swarm database 1979–1989, *U.S. Geol. Surv. Open-File Rep.96-39*.

Brocher, T. A. (2005), Empirical relations between elastic wavespeeds and density in the earth's crust, *Bull. Seismol. Soc. Am.*, *95*(6), 2081–2092.

Chen, and N. Lapusta (2009), Scaling of small repeating earthquakes explained by interaction of seismic and aseismic slip in a rate and state fault model, *J. Geophys. Res.*, *114*, doi:10.1029/2008JB005749.

Chen, and P. M. Shearer (2011), Comprehensive analysis of earthquake source spectra and swarms in the Salton Trough, California, *J. Geophys. Res.*, *116*, doi:10.1029/2011JB008263.

Chen, S. D. Ni, Z. J. Wang, X. F. Zeng, and S. J. Wei (2012), Joint inversion with both local and teleseismic waveforms for source parameters of the 2010 Kaohsiung earthquake, *Chinese J. Geophys.-Ch*, *55*(7), 2319–2328.

Chu, R. S., and D. Helmberger (2013), Source Parameters of the Shallow 2012 Brawley Earthquake, Imperial Valley, *Bull. Seismol. Soc. Am.*, *103*(2a), doi:10.1785/0120120324.

Fuis, G. S., W. D. Mooney, J. H. Healy, G. A. Mcmechan, and W. J. Lutter (1984), A seismic refraction survey of the Imperial-Valley Region, California, *J. Geophys. Res.*, *89*(Nb2), 1165–1189.

Hardebeck, J. L., and A. Aron (2009), Earthquake stress drops and inferred fault strength on the Hayward Fault, East San Francisco Bay, California, *Bull. Seismol. Soc. Am.*, *99*(3), 1801–1814.

Hauksson, E., et al. (2013), Report on the August 2012 Brawley Earthquake Swarm in Imperial Valley, Southern California, *Seismol Res Lett*, *84*(2), 177–189, doi:10.1785/0220120169.

Hill, D. P. (1977), Model for earthquake swarms, *J. Geophys. Res.*, *82*(8), 1347–1352.

Ide, S. (2001), Complex source processes and the interaction of moderate earthquakes during the earthquake swarm in the Hida-Mountains, Japan, 1998, *Tectonophysics*, *334*(1), 35–54.

Ji, C., D. J. Wald, and D. V. Helmberger (2002), Source description of the 1999 Hector Mine, California, earthquake, part I: Wavelet domain inversion theory and resolution analysis, *Bull. Seismol. Soc. Am.*, *92*(4), 1192–1207.

Kagawa, T., K. Irikura, and P. G. Somerville (2004), Differences in ground motion and fault rupture process between the surface and buried rupture earthquakes, *Earth Planets Space*, *56*(1), 3–14.

King, G. C. P., R. S. Stein, and J. Lin (1994), Static stress changes and the triggering of earthquakes, *Bull. Seismol. Soc. Am.*, *84*(3), 935–953.

Klein, F. W., P. Einarsson, and M. Wyss (1977), Reykjanes Peninsula, Iceland, earthquake swarm of September 1972 and its tectonic significance, *J. Geophys. Res.*, *82*(5), 865–888.

Lapusta, N., and J. R. Rice (2003), Nucleation and early seismic propagation of small and large events in a crustal earthquake model, *J. Geophys. Res.*, *108*(B4), no.-2205, doi:10.1029/2001JB000793.

Lohman, R. B., and J. J. McGuire (2007), Earthquake swarms driven by aseismic creep in the Salton Trough, California, *J. Geophys. Res.*, *112*(B4), 10.1029/2006jb004596.

Lynch, D. K., and K. W. Hudnut (2008), The Wister mud pot lineament: Southeastward extension or abandoned strand of the San Andreas fault? *Bull. Seismol. Soc. Am.*, *98*(4), 1720–1729.

Magistrale, H., S. Day, R. W. Clayton, and R. Graves (2000), The SCEC southern California reference three-dimensional seismic velocity model Version 2, *Bull. Seismol. Soc. Am.*, *90*(6), S65–S76.

Plesch, A., C. Tape, and J. F. Shaw (2009), Inversion integration, the San Joaquin Valley and other advances in the community velocity model, paper presented at Southern California Earthquake Center Annual Meeting.

Roland, E., and J. J. McGuire (2009), Earthquake swarms on transform faults, *Geophys. J. Int.*, *178*(3), 1677–1690.

Rubin, A. M. (2008), Episodic slow slip events and rate-and-state friction, *J. Geophys. Res.*, *113*(B11), 10.1029/2008JB005642.

Segall, P., E. K. Desmarais, D. Shelly, A. Miklius, and P. Cervelli (2006), Earthquakes triggered by silent slip events on Kilauea volcano, Hawaii, *Nature*, *442*(7098), 71–74.

Toda, S., R. S. Stein, and T. Sagiya (2002), Evidence from the AD 2000 Izu islands earthquake swarm that stressing rate governs seismicity, *Nature*, *419*(6902), 58–61.

Vidale, J. E., and P. M. Shearer (2006), A survey of 71 earthquake bursts across southern California: Exploring the role of pore fluid pressure fluctuations and aseismic slip as drivers, *J. Geophys. Res.*, *111*(B5), doi:10.1029/2005JB004034.

Vidale, J. E., K. L. Boyle, and P. M. Shearer (2006), Crustal earthquake bursts in California and Japan: Their patterns and relation to volcanoes, *Geophys. Res. Lett.*, *33*(20), doi:10.1029/2006GL027723.

Wei, S. J., et al. (2011), Superficial simplicity of the 2010 El Mayor-Cucapah earthquake of Baja California in Mexico, *Nature Geosci.*, *4*(9), 615–618.

Wicks, C., W. Thelen, C. Weaver, J. Gomberg, A. Rohay, and P. Bodin (2011), InSAR observations of aseismic slip associated with an earthquake swarm in the Columbia River flood basalts, *J. Geophys. Res.*, *116*, doi:10.1029/2011JB008433.